Monthly Notices
of the
ROYAL ASTRONOMICAL SOCIETY

Mon. Not. R. Astron. Soc. **419,** 3304–3318 (2012) doi:10.1111/j.1365-2966.2011.19971.x

The baryons in the Milky Way satellites

O. H. Parry,[1⋆] V. R. Eke,[1] C. S. Frenk[1] and T. Okamoto[1,2]

[1]*Institute for Computational Cosmology, Department of Physics, University of Durham, Science Laboratories, South Road, Durham DH1 3LE*
[2]*Center for Computational Sciences, University of Tsukuba, 1-1-1 Tennodai, Tsukuba, 305-8577 Ibaraki, Japan*

Accepted 2011 October 9. Received 2011 September 29; in original form 2011 May 18

ABSTRACT

We investigate the formation and evolution of satellite galaxies using smoothed particle hydrodynamics (SPH) simulations of a Milky Way (MW) like system, focusing on the best resolved examples, analogous to the classical MW satellites. Comparing with a pure dark matter simulation, we find that the condensation of baryons has had a relatively minor effect on the structure of the satellites' dark matter haloes. The stellar mass that forms in each satellite agrees relatively well over three levels of resolution (a factor of ∼64 in particle mass) and scales with (sub)halo mass in a similar way in an independent semi-analytical model. Our model provides a relatively good match to the average luminosity function of the MW and M31. To establish whether the potential wells of our satellites are realistic, we measure their masses within observationally determined half-light radii, finding that they have somewhat higher mass-to-light ratios than those derived for the MW dSphs from stellar kinematic data; the most massive examples are most discrepant. A statistical test yields an ∼6 per cent probability that the simulated and observationally derived distributions of masses are consistent. If the satellite population of the MW is typical, our results could imply that feedback processes not properly captured by our simulations have reduced the central densities of subhaloes, or that they initially formed with lower concentrations, as would be the case, for example, if the dark matter were made of warm, rather than cold particles.

Key words: methods: numerical – galaxies: evolution – galaxies: formation – cosmology: theory.

1 INTRODUCTION

Substantial progress has been made over the last few years in modelling the formation of galactic dark matter haloes using high-resolution *N*-body simulations (Diemand et al. 2008; Springel et al. 2008; Stadel et al. 2009). Hydrodynamical simulations of such systems inevitably lag behind in terms of resolution, but are now reaching a point where they can be used to investigate the detailed evolution of the baryonic component of satellite galaxies, as demonstrated by several recent studies. Okamoto et al. (2010) studied the effects of different feedback models on the chemical properties and luminosities of the satellite populations around three Milky Way (MW) mass haloes. Okamoto & Frenk (2009) showed that a combination of the early reionization of pre-galactic gas at high redshift and the injection of supernovae (SNe) energy is sufficient to suppress star formation in the myriad of low-mass subhaloes that form in the Λ cold dark matter (ΛCDM) cosmology, confirming results from earlier semi-analytical modelling (Benson et al. 2002; Somerville 2002). Wadepuhl & Springel (2011) further argued that cosmic rays generated by SNe may play an important role in suppressing star formation in satellites.

From an observational point of view, the release of data from the Sloan Digital Sky Survey (SDSS; York et al. 2000) over the last decade has transformed the study of the Local Group satellites. The ∼30 faint dwarf galaxies discovered using those data (e.g. Zucker et al. 2004; Martin et al. 2006; Belokurov et al. 2007; McConnachie et al. 2008) have prompted a new phase of detailed testing of current galaxy formation theories on smaller scales and in more detail than ever before. The SDSS data also reduced the discrepancy that existed between the number of low-mass dark matter haloes predicted by the ΛCDM cosmological model and the number of faint satellites identified around the MW: the 'missing satellite problem' (Klypin et al. 1999; Moore et al. 1999). Over the same period, numerous theoretical models (e.g. Li, De Lucia & Helmi 2010; Macciò et al. 2010; Font et al. 2011) have confirmed early conclusions that a combination of a photoionizing background and feedback processes from SNe is capable of bringing the two into good agreement.

However, it is important to recognize that the satellite problem is not simply a statement that star formation must be suppressed in low-mass haloes. A more subtle but equally important test of any cosmological model is whether the potential wells in which satellite

⋆E-mail: o.h.parry@durham.ac.uk

galaxies form are capable of supporting stellar systems with realistic kinematics. Strigari, Frenk & White (2010) demonstrated that all of the classical MW satellites for which high-quality kinematic data are available are consistent with having formed in dark matter subhaloes selected from the high-resolution ΛCDM *N*-body simulations of the Aquarius project (Springel et al. 2008). However, successful models must satisfy both constraints, producing realistic luminosity functions *and* forming stars in potentials like those inferred from observations.

Boylan-Kolchin, Bullock & Kaplinghat (2011) have recently argued that the most massive subhaloes in high-resolution simulations of CDM haloes are too concentrated to be able to host the brightest observed satellites of the MW. Lovell et al. (2011) have shown that subhaloes formed from warm, rather than cold, dark matter have suitably low concentrations, but both they and Boylan-Kolchin et al. emphasize that other solutions to the discrepancy are possible. One promising possibility is the mechanism originally proposed by Navarro, Eke & Frenk (1996a), whereby the rapid expulsion of dense central gas in a starburst can unbind the inner parts of the halo, significantly reducing its concentration. We find an example of this process in one of the subhaloes formed in the simulations analysed in this paper.

From a theoretical perspective, ab initio hydrodynamic simulations are uniquely well suited to investigate the effects of galaxy formation on the dark matter haloes of satellite galaxies. It has been known for some time that baryons may significantly alter the behaviour of dark matter on some scales. Dissipative processes such as gas cooling, star formation and feedback decouple the dynamical evolution of the baryons from that of the dark matter. The resulting change in the shape of the overall potential in turn affects the phase-space structure of the dark matter halo.

Central concentrations of cold baryonic matter can induce an adiabatic, radial contraction of the central regions (Blumenthal et al. 1986; Gnedin et al. 2004), while the opposite effect can be achieved if dense clumps of baryonic material or inspiralling satellites heat the central distribution of dark matter (El-Zant, Shlosman & Hoffman 2001; El-Zant et al. 2004; Mo & Mao 2004; Mashchenko, Couchman & Wadsley 2006; Mashchenko, Wadsley & Couchman 2008; Goerdt et al. 2010), or if the blowout mechanism of Navarro, Eke and Frenk is effective (see also Gelato & Sommer-Larsen 1999; Mo & Mao 2004; Read & Gilmore 2005; Governato et al. 2010; Pontzen & Governato 2011). This latter mechanism was originally proposed as a means to erase the central dark matter cusps in dwarf galaxies, though whether or not such 'cored' profiles are required by the observations remains a matter of ongoing debate (Goerdt et al. 2006; Sánchez-Salcedo, Reyes-Iturbide & Hernandez 2006; Strigari et al. 2006; Gilmore et al. 2007; Walker et al. 2009). If baryons really do modify the dark matter in satellites on sub-kpc scales significantly, then the value of studying dwarf galaxies with post-processed *N*-body simulations may be very limited.

In this paper, we make use of a model that has already had success in reproducing some properties of the Local Group satellites, including the shape and approximate normalization of their luminosity function and the metallicity–luminosity relation (Okamoto et al. 2010). In Section 2, we outline the details of our simulations, including the initial conditions, simulation code and modelling of various key baryonic physical processes. In Section 3, we expand on the theoretical predictions of the model by examining what effect baryons have had on the dark matter profiles of satellites. We perform tests in Section 4 to ensure that key properties of our satellite population do not depend on the numerical resolution. In Section 5, we compare several observable and derived properties of the simulated satellites to Local Group data. Finally, in Section 6 we discuss the evolution of one particularly interesting satellite in the simulation, which is dominated by its stellar component at $z = 0$. Our main results are summarized in Section 7.

2 THE SIMULATIONS

To investigate the properties of a simulated MW-satellite system, we select one of the six haloes from the Aquarius project described in Springel et al. (2008), halo 'C' in their labelling system. These haloes were extracted from a cosmological simulation in a cube of comoving volume $(100\,\mathrm{Mpc})^3$ and were chosen to have masses close to that of the MW ($\sim 10^{12}\,\mathrm{M}_\odot$) and avoid dense environments (no neighbour exceeding half its mass within $1h^{-1}$ Mpc; Navarro et al. 2010).

As in Aquarius, we employ a 'zoom' resimulation technique, with higher mass boundary particles used to model the large-scale potential and lower mass particles in a $\sim 5\,h^{-1}$ Mpc region surrounding the target halo. Extra power is added to the initial particle distribution on small scales in the high-resolution region, as described by Frenk et al. (1996). We assume a ΛCDM cosmology, with parameters $\Omega_\mathrm{m} = 0.25$, $\Omega_\Lambda = 0.75$, $\Omega_\mathrm{b} = 0.045$, $\sigma_8 = 0.9$, $n_\mathrm{s} = 1$ and $H_0 = 100\,h\,\mathrm{km\,s^{-1}\,Mpc^{-1}} = 73\,\mathrm{km\,s^{-1}\,Mpc^{-1}}$.

The highest resolution realization of halo C in Aquarius had a dark matter particle mass of $1.4 \times 10^4\,\mathrm{M}_\odot$. However, the extra computational time associated with hydrodynamic simulations makes such a resolution impractical; our highest resolution instead corresponds to a dark matter particle mass of $\sim 2.6 \times 10^5\,\mathrm{M}_\odot$ and an initial gas particle mass of $5.8 \times 10^4\,\mathrm{M}_\odot$. In order to conduct convergence studies, we also simulated the halo at two lower resolutions, with particle masses ∼8 and ∼64 times larger. We adopt the same naming convention as Springel et al. (2008), labelling the three runs (in order of decreasing resolution) Aq-C-4, Aq-C-5 and Aq-C-6. Table 1 lists the numerical parameters of each simulation.

Our simulation code is based on an early version of the PM-Tree-SPH code GADGET-3. Baryonic processes are modelled as described in Okamoto et al. (2010), with a number of modifications designed to improve the treatment of SNe-driven winds. In the following subsections, we summarize some of the most important features of the code with emphasis on aspects that have the greatest impact on satellite formation.

2.1 Radiative cooling and the equation of state

Radiative processes in our model are implemented as described in Wiersma, Schaye & Smith (2009a) and include inverse Compton scattering of cosmic microwave background photons, thermal bremsstrahlung, atomic line cooling and photoionization heating from hydrogen and helium. All gas in the simulation volume is ionized and heated by a spatially uniform, time evolving ultraviolet background, as calculated by Haardt & Madau (2001). During the

Table 1. Numerical parameters adopted for the three different resolution simulations: dark matter and gas particle masses and the gravitational softening in physical units.

	M_DM ($\mathrm{M}_\odot$)	M_gas ($\mathrm{M}_\odot$)	ϵ_phys (pc)
Aq-C-4	2.6×10^5	5.8×10^4	257
Aq-C-5	2.1×10^6	4.7×10^5	514
Aq-C-6	1.7×10^7	3.7×10^6	1028

reionization of H and He I ($z = 9$) and He II ($z = 3.5$), an extra 2 eV per atom of thermal energy is added to the gas, smoothed over Gaussian distributions with widths $\Delta z = 0.0001$ and 0.5, respectively, in order to approximately account for non-equilibrium and radiative-transfer effects (Abel & Haehnelt 1999). The contributions to heating and cooling from 11 elements (H, He, C, N, O, Ne, Mg, Si, S, Ca and Fe) are interpolated from tables output by CLOUDY (Ferland et al. 1998), using elemental abundances smoothed over the smoothed particle hydrodynamics (SPH) kernel, to approximate the mixing of metals in the interstellar medium (ISM). This avoids unphysical small-scale fluctuations in the cooling time that arise if the abundances associated with individual particles are used (Wiersma et al. 2009b).

Failure to resolve the Jeans mass (M_J) or Jeans length (λ_J) is known to lead to spurious fragmentation through gravitational instability (Bate & Burkert 1997; Truelove et al. 1997). Techniques employed to avoid this problem typically involve some form of energy injection to maintain an effective pressure that guarantees that the available resolution is sufficient (e.g. Machacek, Bryan & Abel 2001; Springel & Hernquist 2003; Robertson & Kravtsov 2008; Ceverino, Dekel & Bournaud 2010; Schaye et al. 2010). This pressure support has been identified with, for example, a hot phase maintained through energy input by SNe (Springel & Hernquist 2003) and turbulence induced by the disc's self-gravity and rotation (Wada & Norman 2007). We include a minimum pressure explicitly by adopting a polytropic equation of state (EoS) with $P_\mathrm{min} \propto \rho^{\gamma_\mathrm{eff}}$ for gas above the density threshold for star formation and adopt $\gamma_\mathrm{eff} = 1.4$. For $\gamma_\mathrm{eff} > 4/3$, the Jeans mass increases with density (e.g. Schaye & Dalla Vecchia 2008), such that, if it is resolved at the threshold density, it is resolved everywhere. Schaye et al. (2010) showed that, in models where star formation is strongly regulated by stellar feedback, as it is in ours, the choice of γ_eff has very little impact on the global star formation rate. The star formation threshold density is $n_\mathrm{H} > 0.1\ \mathrm{cm}^{-3}$ for the Aq-C-6 simulation and a factor of 4 and 16 higher for the Aq-C-5 and Aq-C-4 simulations, respectively. This scaling is chosen since, for irradiated primordial gas with an isothermal density profile, halving the gravitational softening will increase the maximum density that is resolved by a factor of 4.

2.2 Multiphase ISM and star formation

At sufficiently high pressures, the ISM is known to exist in distinct phases. We follow Springel & Hernquist (2003), modelling gas above the threshold density using hybrid SPH particles, which are assumed to consist of a series of cold clouds in pressure equilibrium with a surrounding hot phase. The total mass in the cold phase can increase through thermal instability and decrease through star formation and cloud evaporation by SNe, but the mass spectrum of clouds is kept fixed as

$$\Phi(m) = \frac{\mathrm{d}N_\mathrm{c}}{\mathrm{d}m} \propto m^{-\alpha}. \quad (1)$$

We adopt $\alpha = 1.7$, guided by observations that suggest a plausible range of 1.5–1.9 (Solomon & Rivolo 1989; Fukui et al. 2001; Heyer, Carpenter & Snell 2001). We follow Samland & Gerhard (2003) in assuming clouds to be spherical, with size at a fixed mass determined solely by the ambient pressure (Elmegreen 1989):

$$\left(\frac{m}{\mathrm{M}_\odot}\right)\left[\frac{r(m)}{\mathrm{pc}}\right]^{-2} = 190 P_4^{1/2}, \quad (2)$$

where $P_4 = \frac{P/k}{10^4\ \mathrm{K\,cm^{-3}}}$ and k is the Boltzmann constant. The dependence of each cloud's dynamical time on the effective pressure follows directly from equation (2):

$$t_\mathrm{dyn} = \left[\frac{3\pi}{32 G \rho(m)}\right]^{1/2} \simeq 0.32 P_4^{-3/8}\left(\frac{m}{\mathrm{M}_\odot}\right)^{1/4} \mathrm{Myr}, \quad (3)$$

and we assume that the star formation rate in each cloud is inversely proportional to its dynamical time (t_dyn):

$$\dot{m}_* = c_* \frac{m}{t_\mathrm{dyn}}, \quad (4)$$

where c_* is the star formation efficiency, which is set to reproduce the normalization of the Kennicutt–Schmidt law (Kennicutt 1998). The total star formation rate for each SPH particle is obtained by integrating equation (4) over all clouds deemed capable of supporting star formation (which we assume to be in the mass range 10^4–$10^6\ \mathrm{M}_\odot$).

SPH particles spawn new collisionless star particles in a stochastic fashion, with a probability that depends on their star formation rate and on the mass in the cold phase. Each star particle represents a single stellar population, forming with a Chabrier (2003) initial mass function (IMF). Energy, mass and metals are returned to the ISM by asymptotic giant branch (AGB) stars, Type Ia and Type II SNe on time-scales appropriate for the age and metallicity of the stellar population, with yields and stellar lifetimes taken from Portinari, Chiosi & Bressan (1998) and Marigo (2001). Rather than performing this calculation at every dynamical time-step, which is very expensive computationally, we use coarser steps, chosen such that the time-scales associated with Type II and Type Ia SNe can be adequately sampled. Initially, each step has length $t_{8\,\mathrm{M}_\odot}/50$, where $t_{8\,\mathrm{M}_\odot}$ is the lifetime of an $8\,\mathrm{M}_\odot$ star.[1] When the age of the stellar population exceeds $t_{8\,\mathrm{M}_\odot}$, the time-steps lengthen to 100 Myr, which is short enough to model the release of mass and energy from Type Ia SNe and from AGB stars.

2.3 Supernovae winds

The perennial problem with the distribution of stellar feedback energy in cosmological hydrodynamical simulations has been that the star-forming gas that receives the energy is dense enough to radiate it away before it can have any dynamical effect (Katz, Weinberg & Hernquist 1996). This is likely to be a consequence of the inability to resolve the detailed structure of the ISM (e.g. Dalla Vecchia & Schaye 2008; Ceverino & Klypin 2009). We employ a commonly used technique to circumvent this limitation, which consists of imparting kinetic energy to gas particles directly (e.g. Navarro & White 1993; Mihos & Hernquist 1994; Springel & Hernquist 2003). The velocity we choose to give gas particles that receive SNe energy is motivated by observations that suggest that large-scale outflows have velocities that scale with the circular velocity of their host galaxies (Martin 2005). As a proxy for the host halo's circular velocity, which is computationally expensive to calculate for each particle on the fly, we use the local 1D velocity dispersion, determined from neighbouring dark matter particles. This quantity is strongly correlated with the maximum circular velocity, v_max, in a way that does not evolve with redshift (Okamoto et al. 2010). Our prescription results in a wind speed that increases as the halo grows and hence, from energy conservation, in a mass loading (wind mass per unit star formation rate) that is highest at early times. This scaling has been shown to give a much better match to the luminosity

[1] $t_{8\,\mathrm{M}_\odot} \sim 40$ Myr at solar metallicity.

function of the MW satellites than models that use a constant wind velocity (Okamoto et al. 2010).

One further addition to the model is needed to ensure that SNe-driven winds act as intended. Dalla Vecchia & Schaye (2008) showed that standard kinetic feedback is more effective in low-mass galaxies, where wind particles tend to drag neighbouring gas out with them. In high-mass galaxies, on the other hand, the pressure of the ISM can be sufficient to prevent much of the mass in the wind from escaping. Since we wish to be able to prescribe the mass loading and wind velocity ($v_{\rm w}$) directly, we choose to decouple wind particles from the hydrodynamic calculation for a short time in order to allow them to escape the high-density star-forming regions. When the density has fallen to $n_{\rm H} = 0.01\,{\rm cm}^{-3}$, the particles feel the usual hydrodynamic force again. If they do not reach sufficiently low densities after a time $10\,{\rm kpc}/v_{\rm w}$, they are recoupled anyway.

When a gas particle receives SNe energy from a neighbouring star particle, the wind speed is obtained from the local velocity dispersion and then the particle is assigned a probability to be added to the wind:

$$p_{\rm w} = \frac{\Delta Q}{\frac{1}{2} m_{\rm sph} v_{\rm w}^2}, \tag{5}$$

where ΔQ is the total feedback energy received by the gas particle and $m_{\rm sph}$ is the current mass of the SPH particle. Note that an SPH particle's mass may increase if it receives mass from SNe or AGB stars in neighbouring star particles, or decrease if it spawns a new star particle, which has a mass of half the original gas particle mass. If $p_{\rm w}$ exceeds unity, that is if there is energy available in excess of that needed to add the particle to the wind, then the extra energy is distributed to the gas particle's neighbours as an increase in internal energy. The direction in which wind particles are propelled is chosen at random to be parallel or antiparallel to the vector $(\boldsymbol{v}_0 - \overline{\boldsymbol{v}}) \times \boldsymbol{a}_{\rm grav}$, where $\boldsymbol{v}_0$ is the velocity of the gas particle before it receives feedback energy, $\boldsymbol{a}_{\rm grav}$ is the gravitational acceleration vector, pointing approximately to the local potential minimum (halo centre) and $\overline{\boldsymbol{v}}$ is the bulk velocity of the halo, which we take to be the mean velocity of the gas particle's dark matter neighbours. The result of this treatment is a wind launched preferentially along an object's rotation axis (Springel & Hernquist 2003). Our model for SNe winds differs from that described by Okamoto et al. (2010) in two ways. First, we allow all gas particles, not just those above the star formation density threshold, to be added to the wind if they receive feedback energy. The original prescription can result in a variable wind mass loading depending on how well the star-forming region is resolved. Secondly, only Type II SNe contribute to the winds, Type Ia SNe energy is added to the gas as thermal energy.

2.4 Fluid instabilities

A known limitation of the standard SPH method is that it tends to suppress instabilities at the contact surfaces between fluids of different specific entropy (e.g. Okamoto et al. 2003; Agertz et al. 2007; Springel 2010; Sijacki et al. 2011). At such boundaries, the density varies smoothly, but entropy is discontinuous, generating spurious pressure forces that prevent effective mixing (Agertz et al. 2007).

Our SPH implementation includes two important features that provide an improved treatment of contact instabilities relative to many other SPH codes. The first is an 'artificial conductivity' prescription, originally introduced by Price (2008). This acts to smooth out entropy across interfaces, reducing the spurious pressure forces that tend to suppress mixing in the standard SPH formulation. Secondly, we employ a time-step limiter similar to that proposed by Saitoh & Makino (2009). Whilst in general the individual time-steps of gas particles are allowed to adapt according to the local density, the limiter specifies that time-steps of neighbouring gas particles cannot differ by more than a factor of 4. This measure was primarily introduced to allow lower density particles to respond properly to shocks, but also improves the modelling of hydrodynamic forces at the interfaces where contact instabilities operate.

Even with these improvements, realistic modelling of contact instabilities requires a very large number of particles (Kawata et al. 2009). We hence expect our code still to provide a somewhat inaccurate treatment and we will highlight instances where this may affect our results.

2.5 Satellite identification

Galaxies are identified using a version of the SUBFIND algorithm (Springel et al. 2001) adapted by Dolag et al. (2009), which identifies self-bound structures and includes the internal energy of gas when computing particle binding energies. From the $\sim$5 Mpc high-resolution region, we select all galaxies within 280 kpc of the centre of the most massive (central) galaxy. This distance was chosen to match the limiting magnitude of the completeness-corrected satellite luminosity function constructed by Koposov et al. (2008). The largest satellite in our Aq-C-4 run is resolved with about 1.5×10^5 particles in total, $\sim 3 \times 10^4$ of which are star particles. In the following, we consider all galaxies with more than 10 star particles, which, taking into account the typical mass fraction lost through stellar evolution for our choice of IMF, implies a stellar mass limit of $\sim 1.2 \times 10^5\,{\rm M}_\odot$ for Aq-C-4.

3 THE EFFECT OF BARYONS ON SATELLITE DARK MATTER HALOES

Using a dark matter only (DMO) counterpart of our Aq-C-4 run, simulated as part of the Aquarius project (Springel et al. 2008), we have examined the extent to which the dynamics of the baryons alter the structure of dark matter (sub)haloes of satellite galaxies over the course of their formation. The DMO run had identical initial conditions to our Aq-C-4, but for the absence of baryons and a correspondingly higher dark matter particle mass by a factor $\sim 1/(1 - \Omega_{\rm b}/\Omega_{\rm m})$.

Naively, one might simply compare each subhalo with its DMO equivalent at $z = 0$, but this turns out to be problematic. As has been noted in previous N-body simulations at different resolutions, small phase deviations in subhalo orbits get amplified over time, such that subhaloes can be in quite different positions at $z = 0$ (e.g. Frenk et al. 1999; Springel et al. 2008). We see similar differences between Aq-C-4 and the DMO run. Subhalo orbits are also affected by other factors such as subhalo–subhalo scattering and variations in the potential due to small differences in the growth history of the main halo.

Since the strength of tidal shocking is strongly dependent on pericentric distance (Gnedin, Hernquist & Ostriker 1999; Mayer et al. 2001), small orbital deviations can cause large differences in subhalo structure, which are entirely unrelated to the presence or absence of baryons. This complication can be avoided, either by choosing subhaloes with no close pericentre or by making the comparison at the epoch when the satellite is first accreted into the halo of the main galaxy, before the orbits have had a chance to diverge. We choose the latter option, since the former restricts us to

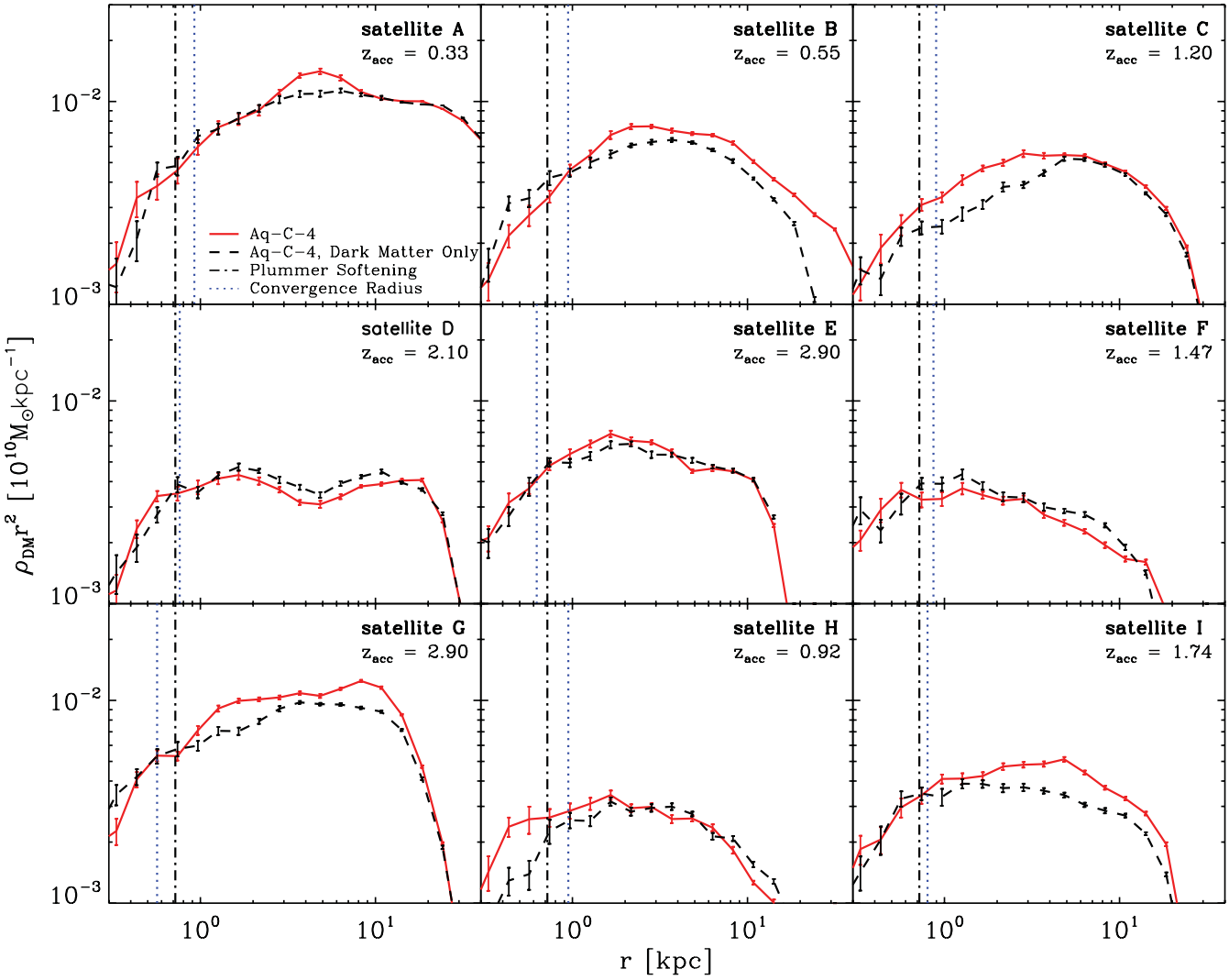

Figure 1. The spherically averaged dark matter density profiles of the nine most massive satellite galaxies in our high-resolution hydrodynamic (red, solid) and DMO (black, dashed) runs. Error bars are obtained by bootstrap resampling. The panels are ordered by total mass in the hydrodynamical run, from left to right along each row, beginning at the top. Identifier labels (A-I) are shown in the top right of each panel, corresponding to the entries in Table 2. The comparisons are made at the redshift where the galaxy is first accreted as a satellite, which is also shown as a label. Black dot–dashed vertical lines indicate the scale on which softened gravitational forces become fully Newtonian. Blue dotted vertical lines indicate the convergence radius of Power et al. (2003).

a very small number of cases, although we note that one massive halo in a low-eccentricity (∼0.2) orbit with a distant pericentre (∼200 kpc) shows comparatively small differences in its dark matter density profile at $z = 0$ relative to the DMO case. In the few instances where the accretion times of the subhalo differ slightly between the hydrodynamical and DMO runs, we choose the earlier of the two epochs.

In Fig. 1, we show spherically averaged profiles for the dark matter density (plotted as ρr^2 to emphasize small differences) of our most massive satellites, for Aq-C-4 and the DMO run at the output time when each satellite first joins the main friend-of-friends (FOF; Davis et al. 1985) group.[2] The differences in the subhalo density profiles with and without baryons clearly exceed the uncertainties associated with finite sampling, indicated by the error bars. They are also greater than, for example, the differences expected between dark matter realizations of the same subhalo at different resolutions (Springel et al. 2008). Some subhaloes (e.g. top left and centre right panels) appear to have been largely unaffected, whilst others (e.g. top and bottom right panels) show more substantial changes of up to 30 per cent in some radial bins. In Section 6, we describe an extreme example of a subhalo which suffered much more extensive damage as a result of baryonic processes. In general, however, there does not seem to be any consistent trend for baryons to increase or decrease the central density of the dark matter.

In Fig. 2, we show spherically averaged dark matter velocity dispersion profiles for the same selection of satellites in Aq-C-4 and the DMO run. The largest differences are seen in those subhaloes that show the most change in their density profiles in Fig. 1. Once again, the differences are typically less than 10 per cent in any given radial bin, but as much as 30 per cent in some instances, with no apparent trend for baryons to raise or lower the dark matter velocity dispersion.

From these results, we conclude that the baryons have had a relatively small impact on the dark matter phase-space structure of

[2] In practice, we require the subhalo to be counted in the main FOF group for two consecutive snapshots to avoid instances where subhaloes are spuriously joined to the main group for a short time.

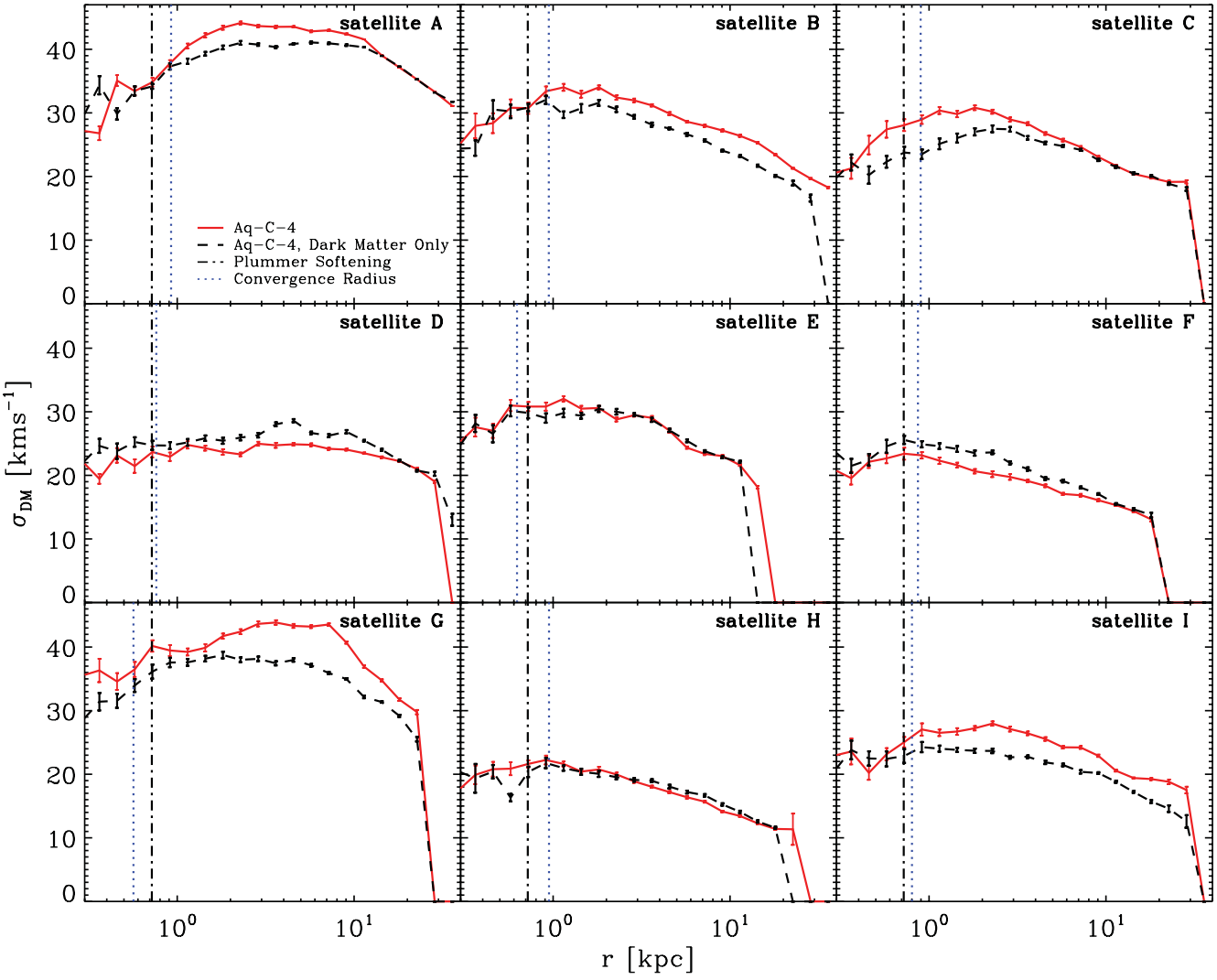

Figure 2. The spherically averaged 1D velocity dispersion profiles of the most massive satellite galaxies in our high-resolution hydrodynamic (red, solid) and DMO (black, dashed) runs. Error bars are obtained by bootstrap resampling. The comparisons are made at the redshift when the galaxy is first accreted as a satellite, which is indicated on the corresponding panels in Fig. 1. Black dot–dashed vertical lines indicate the scale on which softened gravitational forces become fully Newtonian. Blue dotted vertical lines indicate the convergence radius of Power et al. (2003).

the subhaloes, with the important caveat that it is unclear whether such effects are limited by the resolution of our simulations. Whilst this conclusion applies to most subhaloes, an exception that will be discussed in Section 6 exhibits the blowout mechanism studied by Navarro, Eke & Frenk (1996a), Gelato & Sommer-Larsen (1999), Read & Gilmore (2005), Governato et al. (2010) and Pontzen & Governato (2011) which decreases the central dark matter density relative to the non-dissipative run. Another important factor contributing to our conclusion is the strength of our feedback, since it dictates how easily baryons are able to condense in the centre of low-mass haloes and affect the dynamics of the dark matter. Models with much weaker feedback might result in more pronounced differences than we see here, but as we will show in Section 5.1, such models typically overpredict the luminosities of satellite galaxies.

Although some satellites are accreted at fairly high redshift (see the labels on each panel in Fig. 1), it is unlikely that the baryons would have an increased effect in the remaining time to $z = 0$. In all but the largest satellites, gas is lost fairly rapidly following accretion, as we will show in Section 4.2.

4 CONVERGENCE OF SATELLITE PROPERTIES

In this section, we investigate the convergence of various key properties of our simulated satellite galaxies. We make the comparison on an object-to-object basis, matching up satellites between runs. As explained in Section 3, this cannot be accomplished simply by choosing subhaloes that are spatially closest at the final time. Instead, we trace particles back to the initial conditions and match them spatially there. In the following analysis, we consider the most massive satellites in Aq-C-4 for which resolved counterparts exist in Aq-C-5 and often also in Aq-C-6.

4.1 Stellar mass

We begin by considering the total stellar mass in each satellite at $z = 0$. This is a function of the rate at which gas can cool on to the galaxy and the efficiency of star formation, dictated by the gas physics and feedback. As well as checking that our results do not depend on resolution, we compare with an independent

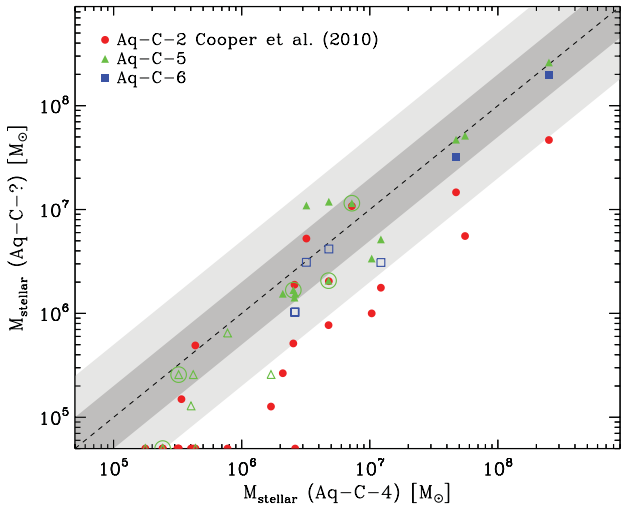

Figure 3. A comparison of the stellar mass that forms in each satellite at the three different resolutions of our hydrodynamical runs, as well as in the independent semi-analytical model presented by C10. Note that not all satellites in the high-resolution run have resolved counterparts at intermediate and low resolution. Points that lie on the abscissa correspond to subhaloes with $M_{\rm stellar} < 5 \times 10^4\,{\rm M}_\odot$ in the corresponding run. Data points are plotted for all satellites in the high-resolution run with more than 10 star particles. If the satellite also has 10 star particles in the lower resolution run, it is plotted as a filled, rather than open symbol. Satellites that have lost more than 50 per cent of their maximum stellar mass through tidal stripping are indicated by circled points. The dark and light grey shaded regions represent factors of 2 and 5, respectively, away from the line of equality.

modelling technique, presented by Cooper et al. (2010, hereafter C10). They used the Aquarius simulations to track the formation of dark matter substructures in six different haloes and a version of the semi-analytical galaxy formation code GALFORM to compute the baryonic properties of satellite galaxies.[3] At each output time, the stellar mass formed since the last simulation snapshot is assigned to some fraction of the most tightly gravitationally bound dark matter particles in the subhalo, providing spatial and kinematic information for the stars. The 'tagged' fraction was chosen to match the distribution of sizes (half-light radii) for Local Group satellites and also to produce results robust to changes in resolution.

Fig. 3 demonstrates that the stellar mass in each subhalo agrees relatively well between the three resolutions, particularly for the most massive examples, although the difference is as large as a factor of 6 in one case. Some of this scatter (between different resolutions and between the semi-analytical and hydrodynamical realizations) is likely related to the deviations in subhalo orbits between simulation runs described in Section 3. Small differences in pericentric distance and eccentricity can strongly affect the tidal field and hence the extent to which stars can be stripped from subhaloes. Examples of subhaloes that have lost more than 50 per cent of their peak stellar mass (excluding the effects of stellar evolution) in one or more of the runs are indicated in Fig. 3 by circled points.

[3] Their semi-analytical model is essentially that presented by Bower et al. (2006), but with a lower circular velocity threshold ($30\,{\rm km\,s^{-1}}$) to identify haloes in which cooling is suppressed by reionization. This value is motivated by recent hydrodynamical simulations (Hoeft et al. 2006; Okamoto, Gao & Theuns 2008).

The semi-analytical prescription typically predicts a lower stellar mass in each subhalo, although the correlation indicates that the ranking of subhaloes by stellar mass is similar to that in our simulations. This offset between the two techniques is not obviously attributable to a single aspect of either model, but one mechanism that may be important is ram pressure stripping. In the semi-analytical model, any hot gas is instantaneously stripped from satellites upon infall. In combination with strong SNe feedback, this quenches star formation in satellites very rapidly following accretion. As we will show in the next subsection, ram pressure and feedback act to produce a similar effect in our simulations, but star formation is able to continue for an appreciable time after accretion and right up to $z = 0$ for the most massive satellites.

4.2 Mass evolution

We now examine how satellites in the three runs acquire their dark and baryonic mass and form stars. Fig. 4 shows the gravitationally bound mass of dark matter, stars and gas for the nine most massive satellites as a function of redshift. For reference, we also include Table 2, which lists the masses at $z = 0$. Reionization ($z = 9$) is marked with a vertical dot–dashed line and arrows indicate the accretion time, that is the epoch when the galaxy first becomes a satellite in the high-resolution run. Where the accretion times differ slightly between runs, the value for the high-resolution case is shown. We note that the exact values plotted in Fig. 4 and listed in Table 2 are sensitive to the manner in which the 'edge' of each subhalo is defined. As demonstrated by Knebe et al. (2011b), when subhaloes lie close to the centre, SUBFIND can underestimate their total mass by up to 30 per cent relative to other halo-finding algorithms, assigning some of the particles in their outer parts to the main halo. This effect is, in fact, visible in the dark matter masses of some of the satellites, which increase slightly after pericentre as particles are reassigned to them. None the less, this feature does not impact on the general trends illustrated in Fig. 4.

Apart from numerical convergence, which we will discuss next, there are a number of interesting features to note in Fig. 4, many of which were also observed in the simulations of Okamoto et al. (2010), Wadepuhl & Springel (2011) and Sawala, Scannapieco & White (2011). There are instances of satellites being periodically stripped of mass as they pass through pericentre, most obviously the satellite tracked in the bottom right panel, which loses dark matter and gas from its outer parts in two close approaches. None of these massive satellites appears to be on orbits with sufficiently high eccentricity and/or a close pericentre to strip the more tightly bound stellar component significantly, although there are several examples of satellites in the simulation that were heavily stripped or disrupted entirely and hence are not among the most massive at $z = 0$.

The loss of gas following accretion in most cases is fairly rapid and is brought about through a combination of ram pressure stripping and stellar feedback. The effectiveness of ram pressure stripping is known to be underestimated by SPH codes, due to the suppression of Rayleigh–Taylor and Kelvin–Helmholtz instabilities that should develop between infalling gaseous structures and their associated bow shocks (Agertz et al. 2007). Although the numerical measures described in Section 2.4 mitigate this problem, the gas content and star formation rates of satellites after accretion are likely to be overestimated somewhat. Extreme upper limits for the overestimate can be determined by the fraction of the final stellar mass of each satellite that forms after accretion. This is typically

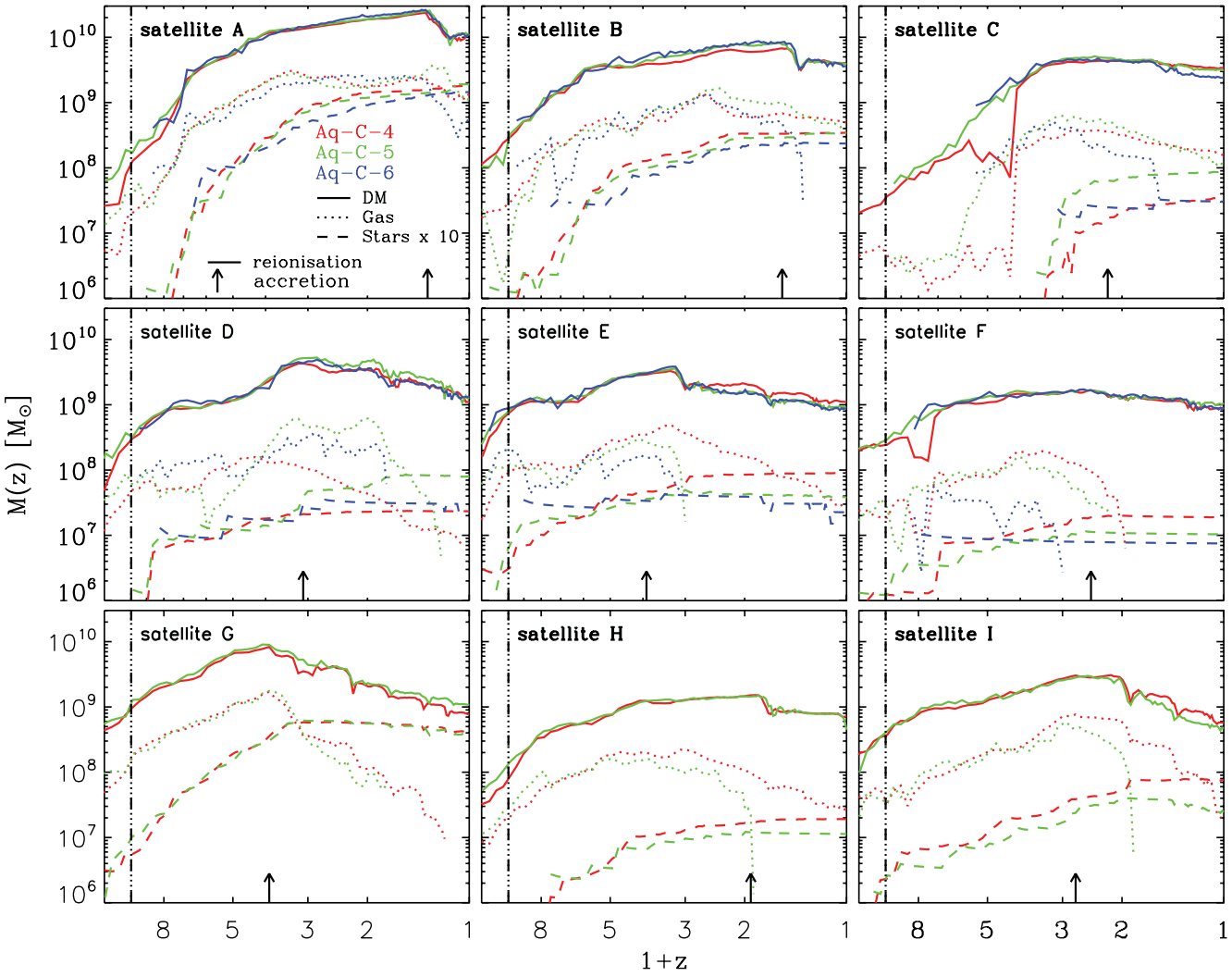

Figure 4. The mass evolution in dark matter (solid lines), stars (dashed lines) and gas (dotted lines) for the nine most massive satellite galaxies in our Aq-C-4 (red), Aq-C-5 (green) and Aq-C-6 (blue) simulations. Note that no resolved counterpart was identified in the Aq-C-6 simulation for the satellites tracked in the bottom row of panels. Stellar masses are scaled up by a factor of 10 to reduce the range of the ordinate axis. The vertical dot–dashed line indicates the redshift of reionization and arrows the epoch at which the galaxy was first accreted as a satellite in Aq-C-4. The panels are ordered by total mass, from left to right along each row, beginning at the top.

Table 2. The mass in dark matter, gas and stars gravitationally bound to the nine most massive satellites at $z = 0$. The identifier labels (left-hand column) correspond to those shown on each panel of Figs 1, 2 and 4.

Label	$M_{\rm DM}$ ($10^6\,{\rm M}_\odot$)	$M_{\rm gas}$ ($10^6\,{\rm M}_\odot$)	M_* ($10^6\,{\rm M}_\odot$)
A	14 822.3	1734.8	250.5
B	14 236.2	584.1	27.7
C	5436.6	678.1	47.2
D	4634.8	215.2	4.8
E	1548.1	0.0	3.2
F	1496.5	40.6	12.2
G	1229.1	0.0	2.6
H	1049.7	0.0	55.4
I	1001.8	37.6	2.6

less than 15 per cent, but it can be as high as 50 per cent in a few of the more massive examples.

As noted by both Okamoto & Frenk (2009) and Wadepuhl & Springel (2011), reionization appears to have virtually no impact on satellites this large (the lowest mass example in Fig. 4 has final total mass of $5 \times 10^8\,{\rm M}_\odot$); the gas mass rises steadily through $z = 9$, and star formation continues unabated. We note that the three largest satellites retain a substantial amount of gas and are still increasing their stellar mass at the present day, analogously to the ongoing star formation in the MW dIrrs.

In terms of numerical convergence, in most respects, there is good agreement between the three resolutions. The exceptions to this are the rate at which gas is lost from some satellites following accretion and the resulting effect on the late-time star formation rates. In most cases, there is a clear tendency for more efficient ram pressure stripping with decreasing resolution. This effect is related to the force resolution, which results in gas particles in lower resolution

runs being less tightly bound and hence more susceptible to ram pressure stripping. The slightly different time-scales over which satellites are able to retain their gas and continue to form stars account, at least in part, for the often lower final stellar masses in Aq-C-5 and Aq-C-6 noted in the previous subsection.

5 OBSERVED PROPERTIES

In the previous section, we demonstrated that our model produces satellite galaxies with properties that show reasonable convergence with resolution and stellar masses that scale with subhalo mass in a fashion expected from an alternative modelling technique. We now proceed to examine how well their observable properties match those of the Local Group satellites. Where photometric quantities are required, we use the stellar population synthesis model PEGASÉ (Fioc & Rocca-Volmerange 1997), summing the luminosities of all star particles gravitationally bound to the subhalo at $z = 0$.

5.1 Satellite luminosity function

One of the most fundamental properties of any galaxy population is its luminosity function. Encoded in its shape and normalization are a range of physical processes that are key to understanding the formation and evolution of the population.

In Fig. 5, we plot the luminosity function of simulated satellites at each resolution. Also plotted is the (completeness-corrected) average luminosity function for MW and M31 satellites from Koposov et al. (2008) that includes the SDSS ultrafaint objects. We find good agreement between resolutions at all resolved luminosities, consistent with the convergence of stellar masses and star formation histories demonstrated in Section 4. The simulated populations provide good matches to the Local Group average at the faint end, consistent with the findings of Okamoto et al. (2010) in another of the Aquarius haloes, but have no galaxy as bright as the Large Magellanic Cloud (LMC). The brightest galaxy (in Aq-C-4) has a similar V-band magnitude to that of the Small Magellanic Cloud (SMC). In the previous subsection, we noted that ram pressure stripping is likely to be underestimated, such that the gas reservoirs of satellites should be depleted more quickly and their final luminosities should be lower. For the model parameters used in these simulations, this would slightly increase the disagreement with the observed luminosity function at the bright end. Alternatively, it implies that less feedback energy would be required in order to obtain a reasonable match to the luminosity function.

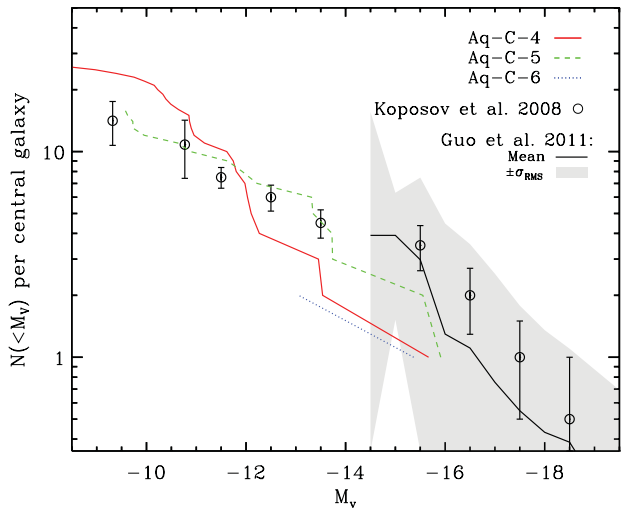

Figure 5. The rest-frame, V-band luminosity function of satellite galaxies in our high- (red, solid), intermediate- (green, dashed) and low-resolution (blue, dotted) simulations. Circles with error bars indicate the average MW+M31 satellite luminosity function, corrected for completeness, by Koposov et al. (2008). Note that this correction is negligible for all but the extreme faint end of the magnitude range plotted here. For consistency with their data, only simulated satellites within 280 kpc of the central galaxy are included. The solid black line and grey shaded regions indicate the mean and spread in the satellite luminosity functions of MW mass galaxies in an analysis of SDSS data by Guo et al. (2011). The light grey region shows the rms scatter about the mean in each bin.

Note that there is still a significant observational uncertainty in the total mass of the MW. Current estimates put it between 0.8 and $3 \times 10^{12}\,\mathrm{M}_{\odot}$ (Dehnen, McLaughlin & Sachania 2006; Li & White 2008; Xue et al. 2008; Watkins, Evans & An 2010). Our halo has a mass slightly closer to the lower end of this range of $M_{\mathrm{crit},200} = 1.42 \times 10^{12}\,\mathrm{M}_{\odot}$. Clearly, if we are simulating a halo twice or half as massive as the MW, we should not expect to reproduce the luminosity function of its satellites exactly. A further consideration is whether the MW has a typical satellite population for its halo mass or total luminosity. To this end, we have also plotted a black solid line and shaded region indicating the mean and spread of the luminosity function (see figure caption for details) for satellite systems in the SDSS around central galaxies with r-band luminosity close to that of the MW (Guo et al. 2011). These data suggest that the Local Group is fairly typical, although satellites like the Magellanic Clouds are found in fewer than half of the systems in the sample. In another study, Liu et al. (2011) found that >80 per cent of MW-like galaxies have no satellite as bright as the SMC within 150 kpc. Tollerud et al. (2011) used SDSS data to derive a statistic that is more readily compared to the data plotted in Fig. 5, namely that 42 per cent of $\sim L_*$ galaxies have a satellite with $0.1L_* \leq L \leq L_*$ within a (projected) distance of 250 kpc. Hence, while LMC/SMC analogues at these large projected radii may not be rare, the lack of very bright satellites in our simulations is not a major cause for concern.

5.2 Sizes

An important and readily observable property of the most massive Local Group satellites is the distribution of their sizes, usually measured as the radius containing half the luminosity in projection. Unfortunately, a combination of the spatial resolution and the limitations of our subgrid model for star formation means that we cannot hope to reproduce the observed sizes in our simulations. As explained in Section 2, a minimum pressure is maintained in star-forming gas to ensure that the Jeans length on the EoS, $\lambda_{\mathrm{J,EoS}}$, is always resolved. Our subgrid model assumes that stars form on much smaller (unresolved) scales, inside molecular clouds, but the star particles that are created must none the less inherit the dynamical properties of the SPH particle from which they formed. As a result, the minimum size of star-forming regions will be dictated by the warm/hot phase density and temperature, through $\lambda_{\mathrm{J,EoS}}$, or by the gravitational softening, if this is larger.

These limits are apparent in Fig. 6, where we plot the absolute V-band magnitude of simulated satellites as a function of their half-light radius. The observed half-light radii are deprojected by multiplying by a factor of 4/3, an approximation that is accurate to 2 per cent for the exponential, Gaussian, King, Plummer and Sérsic profiles commonly used to fit the MW satellites (Wolf et al. 2010). The stars in both the Aq-C-4 and Aq-C-5 runs typically have much less concentrated distributions than the observed satellites. An

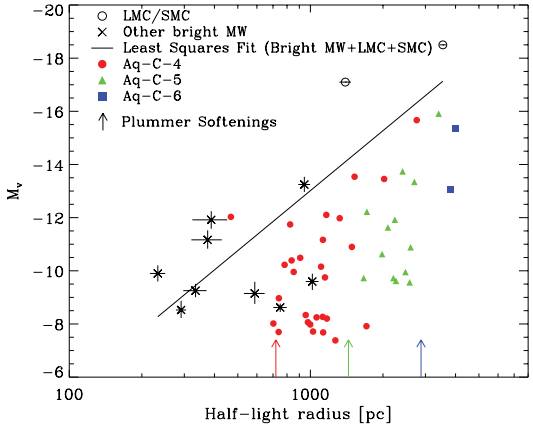

Figure 6. Absolute V-band magnitude as a function of deprojected half-light radius for satellite galaxies in our Aq-C-4 (red filled circles), Aq-C-5 (green filled triangles) and Aq-C-6 (blue filled squares) runs. The Magellanic Clouds are represented by black circles. Their projected half-light radii were derived from angular values taken from Bothun & Thompson (1988) and distance estimates from Hilditch, Howarth & Harries (2005) and Pietrzyński et al. (2009). 3D half-light radii were calculated by multiplying these values by 4/3, as suggested by Wolf et al. (2010). All other MW satellites brighter than −7.5 (except Sagittarius) are shown as black crosses; their luminosities and deprojected half-light radii are taken from Wolf et al. (2010). The solid black line is a least-squares fit to all the observational data points. Arrows indicate the scales on which softened gravitational forces become fully Newtonian for each resolution.

exception to this is the third brightest satellite in Aq-C-4, which has a V-band magnitude of −12.2 and a half-light radius of ∼480 pc. It has a very high mass fraction in stars and an unusual history, forming in a series of violent major mergers at $z \sim 4$ before being subjected to strong tidal disruption between $z = 2$ and 0. We discuss this satellite in detail in Section 6.

In the highest resolution run, Aq-C-4, we expect the gravitational softening to be the main factor limiting the minimum sizes of star-forming regions, since it is always larger than $\lambda_{\rm J,EoS}$. In Aq-C-5 and Aq-C-6, which have lower threshold densities for star formation by factors of 4 and 16, respectively, $\lambda_{\rm J,EoS}$ at the threshold is comparable to the softening, so should also be important in setting the sizes of the stellar component. For both Aq-C-4 and Aq-C-5, the half-light radius of the most massive galaxy should not be limited by either effect and is consistent with the observations, given the large scatter.

5.3 Dynamical masses

The stellar kinematical properties of Local Group dwarf galaxies provide an important test of the ΛCDM cosmology. Subhaloes that form in N-body simulations of MW-mass systems appear to have potentials compatible with the stellar kinematics of the brightest MW satellites (Stoehr et al. 2002; Strigari et al. 2010). None the less, the analytic calculations required to reach such conclusions necessarily include simplifying assumptions. Hydrodynamic simulations attempting to model star formation self-consistently in a cosmological setting are inevitably some way behind the best N-body simulations in terms of resolution and must also model uncertain baryonic physics on sub-kpc scales. As such, our simulations are not suitable for studying the detailed kinematics of the stars directly; instead, we resort to a somewhat cruder comparison and ask whether our satellites form in realistic potential wells, by comparing simulated and observationally determined masses.

Historically, there has been significant uncertainty associated with determining satellite masses from observations. Typically, estimates are derived from the line-of-sight stellar velocity dispersion with three key assumptions: (i) the system is spherically symmetric, (ii) stellar orbits are isotropic and (iii) the system is in equilibrium. Two recent studies have attempted a more general approach, with the aim of reducing the systematic uncertainties. Using an approach based on the spherical Jeans equation, Walker et al. (2009) showed that for the brightest MW dSphs, the mass within the projected half-light radius is robust to changes in the anisotropy and underlying density profile. This relation was explained analytically by Wolf et al. (2010), who demonstrated that, if the stellar velocity dispersion profile remains relatively flat in the centre, as observations suggest (e.g. Walker et al. 2007), then the uncertainty introduced by assuming a particular anisotropy is minimized at the (3D) radius where the logarithmic slope of the stellar number density profile $-{\rm d}\ln n_*/{\rm d}\ln r = 3$. They also showed that, for a range of realistic light profiles that have been used to model the MW dSphs, this minimum lies close to the (deprojected) half-light radius. It is this radius, therefore, at which we choose to compare the enclosed masses of satellites in the simulations and observations.

In the previous subsection, we described how aspects of our simulations, particularly the limitations of the subgrid treatment of the ISM and the gravitational softening scale, can set an artificial lower limit to the sizes of the stellar components of the satellites. However, we also demonstrated that the luminosity function of the simulated satellites is close to that observed, the stellar mass in each satellite is relatively well converged and stellar mass is found to scale with subhalo mass similarly using an alternative modelling technique.

With these checks in mind, we proceed with the assumption that the cooling, star formation and feedback prescriptions in our model result in a realistic stellar mass in each satellite, but that stars form in a configuration that is too diffuse. We then ask what the projected half-light radius of each simulated satellite *should be* at a fixed luminosity, based on the observed sizes of the brightest MW satellites. We take a simple least-squares fit to the data points in Fig. 6 (minimizing the sum of the squared differences in the magnitude coordinate) and compute the scatter in the (log) radius coordinate about this line. For each simulated satellite, we assume a Gaussian distribution of possible sizes, with a mean equal to the fit evaluated at the satellite's luminosity and dispersion defined by the observed scatter.

Following this procedure, we find that, for magnitudes $M_V > -12$, our fit to the observed data implies sizes below the scale at which softened gravitational forces become non-Newtonian in the Aq-C-4 simulation, which leads to an underestimation of the enclosed mass. We choose instead to measure the mass of each satellite in a much higher resolution DMO realization of the simulation, Aquarius-C-2, which has a smaller softening scale by a factor of ∼4, such that the fitted half-light radii of satellites down to $M_V \sim -7.5$ are larger than the force resolution. The central masses measured in the higher resolution simulation are typically 40 to 80 per cent higher for the 10 brightest satellites, but the difference can be a factor of 3 for satellites with $M_{\rm V} \sim -8$. Given the results presented in Section 3, we do not expect the omission of baryons from Aquarius-C-2 to have had a large impact on the central densities and hence the measured masses of these satellites.

Fig. 7 shows the mass enclosed within the mean half-light radius chosen for each satellite, with error bars indicating the masses corresponding to $\pm 1\sigma$ sizes. Although the range of plausible values is large, the brightest simulated satellites have mean masses three

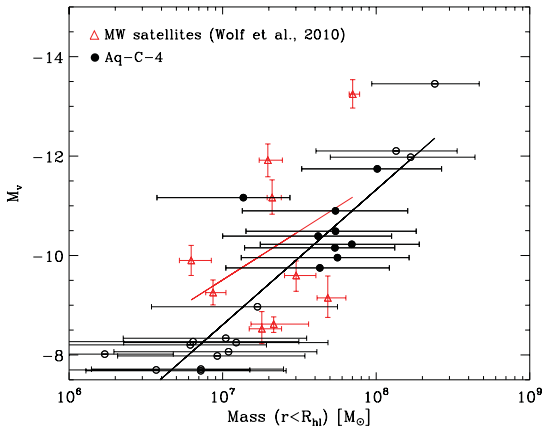

Figure 7. The total mass contained within the projected half-light radius ($R_{\rm hl}$) of simulated satellites, measured in the high-resolution, DMO, Aquarius-C-2 simulation (open and filled black circles). The radii are inferred from the observed luminosity–size relation (see text for details). The filled circles indicate those satellites that are used in the statistical comparison with the observed data, illustrated in Fig. 8. The error bars on the simulated data points show the masses obtained by assuming half-light radii 1σ above and below the mean fitted values, where σ is determined by the scatter about the fit to the observed data. Red crosses with error bars are estimates from Wolf et al. (2010) for a selection of MW satellites. Black and red lines show least-squares fits to the simulated and observed data points, respectively.

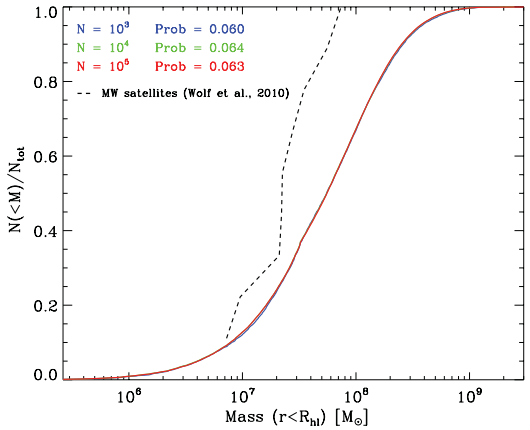

Figure 8. The cumulative fraction of the fourth to 12th brightest satellites as a function of the mass contained within the half-light radius in three model distributions (solid blue, green and red lines) and those derived for MW satellites by Wolf et al. (2010) (dashed line). Labels in the top left indicate the number of times we repeat the process of drawing masses for our sample of nine satellites in order to define the model distribution, along with the probability that each model is consistent with the observed masses.

to five times higher than the MW satellites of the same luminosity. While there is less of a discrepancy at fainter magnitudes, our model seems to show a more gradual increase in luminosity with mass than is suggested by the observational data. We note that, starting from identical initial conditions to our Aq-C-4 simulation, Wadepuhl & Springel (2011) found that the mass-to-light ratios of their satellites were typically higher than those quoted observationally by a very similar factor and were also more discrepant in the most massive satellites (see their fig. 15). In a hydrodynamic simulation of the Local Group, again with resolution similar to our Aq-C-4, Knebe et al. (2011a) found a similar result for satellites bound to their MW and M31 analogues, with mass-to-light ratios a factor $\sim$7 too high. We note, however, that they measured half-light radii for their satellites using the star particles forming in their simulation, which, as we have shown, can be too large when the scales associated with star formation are not resolved.

To quantify the discrepancy in Fig. 7 statistically, we construct multiple realizations of the half-light masses of the simulated satellites by drawing sizes from the distributions described above and computing the mass enclosed in the corresponding high-resolution Aquarius-C-2 satellites. We then combine the samples to define a model distribution for the cumulative fraction of satellites with mass larger than a given value and calculate the probability that the observed masses could have been drawn from it, using a one-tailed Kolmogorov–Smirnov (KS) test (Kolmogorov 1933; Smirnov 1939).

In order to make a like-for-like comparison with the results of Wolf et al. (2010), who did not measure masses for the Magellanic Clouds or Sagittarius, we exclude the three brightest simulated satellites from our analysis. At the faint end, our selection is dictated by resolution: we do not consider the faintest galaxies, i.e. those with fewer than 10 star particles. These choices restrict our sample to the fourth to 12th brightest satellites, which are indicated in Fig. 7 by filled circles. Note that the third brightest satellite in Aq-C-4 is in the midst of tidal disruption (see Section 6), a process that, as a result of small differences in the orbits of the subhaloes, is already complete in Aquarius-C-2, hence no counterpart is found. In Fig. 8, we plot cumulative model distributions, drawing masses for the sample of nine satellites multiple times to define each distribution, as indicated by the labels in the top left of the plot. The probability that the observationally derived masses are consistent with those distributions is found to be around 6 per cent. Note that this result is relatively insensitive to small changes in the luminosities of the satellites, such as those that may result from underestimating the effects of ram pressure stripping. Lower luminosities also decrease the half-light radius assigned to each satellite and hence the mass enclosed, moving the simulated points in Fig. 7 approximately parallel to the line of best fit.

As both Figs 7 and 8 demonstrate, the masses of the brightest simulated satellites are too high compared to those derived for the MW satellites. This is another manifestation of the problem recently highlighted by Boylan-Kolchin et al. (2011) who compared the measured masses within the half-light radii of the same satellites considered here with results from high-resolution simulations of CDM haloes, including the Aquarius suite. Assuming an NFW density profile (Navarro, Frenk & White 1996b, 1997), they showed that the most massive subhaloes in the simulations are too concentrated to be able to host the brightest observed satellites.

The mismatch seen in Fig. 7 and in the results of Boylan-Kolchin et al. (2011) could, in principle, be due to an underestimate of the central masses of the observed satellites. However, for the errors quoted by Wolf et al. (2010) to be substantially underestimated would require rather extreme variations in the anisotropy profile, which would be poorly fit by their fairly general parametrized form. This seems unlikely to be the sole source of the disagreement between model and data.

While the discrepancy could be simply due to statistics, it might also reflect a serious shortcoming either of the standard CDM cosmogony or of current models of galaxy formation, such as those assumed in our simulations. A possible explanation of the discrepancy between the mass-to-light ratios measured for the real and simulated satellites is that the central dark matter densities predicted in the CDM model are reduced by baryonic physics. One

mechanism for achieving this, proposed by Navarro et al. (1996a), is the condensation of a dense baryonic component followed by the rapid expulsion of gas by stellar feedback. The dark matter adjusts to this change in the potential by developing a central 'core', shifting the rotation curve maximum to a larger radius and reducing the mass-to-light ratio in the central parts. This process does indeed appear to play an important role in the evolution of one satellite in Aq-C-4 (see Section 6), which forms in the subhalo that has the largest mass prior to accretion. If this process is common, it is possible that it is not seen here in less massive subhaloes due to lack of resolution.

A more radical explanation of the discrepancy is that the dark matter consists of warm, rather than cold, particles. In this case, subhaloes of a given mass form later and have lower concentrations than in the CDM model (see Navarro et al. 1997; Hogan & Dalcanton 2000). Lovell et al. (2011) have recently shown explicitly that the masses and concentrations of subhaloes in a warm dark matter model agree well with the data.

6 A STAR-DOMINATED SATELLITE

The formation history of one of the satellite galaxies in our high-resolution hydrodynamical simulation is particularly interesting. By $z = 0$, we find that it has become dominated by its stellar component, with a mass-to-light ratio of $\sim$2.4 and its dark matter has become much less concentrated than otherwise similar subhaloes. It appears as an outlier in Fig. 6, as it has a very small half-light radius for its luminosity. In this section, we briefly describe its formation history and explain why it develops into such an unusual object.

At $z = 0$, the satellite is, in fact, in the process of being tidally disrupted and has a substantial stellar stream associated with it. Fig. 9 illustrates the structure of the stream in two orthogonal projections centred on the main galaxy. The dense stellar nucleus of the satellite that remains identifiable as a bound structure is also visible. We track all star particles associated with the satellite at the epoch when it is accreted and plot their projected mass density at $z = 0$. The stripped stars account for the majority of the stellar halo by mass.

The stream is a result of a fairly eccentric orbit with several close pericentres, illustrated in the bottom panel of Fig. 10, which shows the distance of the satellite from the centre of the main galaxy as a function of redshift. The dashed line indicates the virial radius of the main halo. The accretion time is the point where the two lines intersect. The top panel tracks the mass in gas, dark matter and stars bound to the satellite over the same redshift interval, as well as the total mass fraction in stars. At accretion, it is the brightest satellite of the central galaxy, but only the third brightest at $z = 0$, as a result of the reduction in stellar mass through tidal stripping. The stellar fraction at accretion ($\sim$0.02) is fairly typical of the surviving satellites. Note that it is very common for the stellar fraction of a satellite to increase with time after it is accreted, since the outer parts of the dark matter halo are less tightly bound than the stars and hence more susceptible to tidal stripping (e.g. Peñarrubia, Navarro & McConnachie 2008; Sawala et al. 2011). The middle panel of Fig. 10 shows the evolution of the central ($r < 1$ kpc) density of the subhalo in gas and dark matter, both of which drop sharply when the satellite is close to pericentre. A decline is also evident after $z \sim 3$, well before the satellite is accreted, the origin of which we discuss in more detail below.

During the first few orbits, the stellar component remains unaffected, while the dark matter lying beyond the radial extent of the stellar component is stripped. In fact, some of the dark matter particles with pericentres *within* the stellar component are also stripped, as a result of the dark matter having a higher radial velocity dispersion than the stars. The final masses of the stellar and dark matter components are factors of $\sim$50 and 2×10^4 lower than their peak values, respectively.

The extent to which the two components are stripped is strongly affected by their radial density profiles, which are shown in Fig. 11 at the time of accretion. The overplotted regions indicate the range of densities ($\pm 1\sigma$) in each bin for the nine most massive surviving satellites. Clearly, the stellar component of this galaxy is unusually concentrated relative to those other galaxies, whilst the dark matter

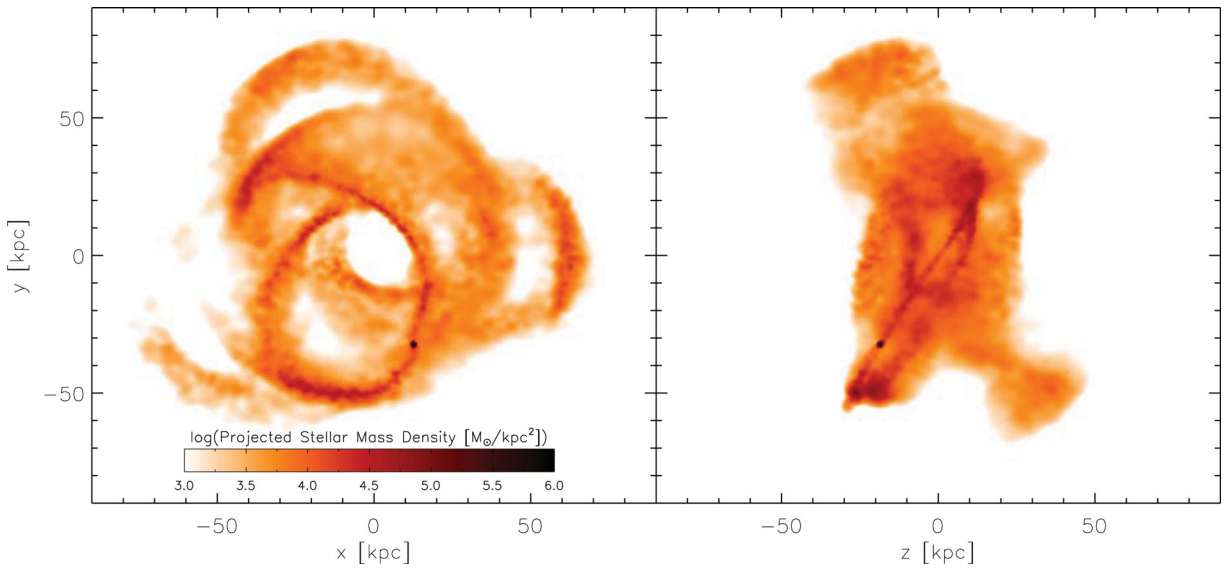

Figure 9. Two orthogonal projections through a cube of side 180 kpc, centred on the potential minimum of the main halo, showing the stellar stream associated with the satellite. Projected stellar mass density is plotted on a white–red–black scale as indicated by the colour bar. The stream is defined by selecting all stars associated with the satellite at the time of accretion and locating them at $z = 0$. The surviving satellite is clearly seen as the dark concentrated object lying along the stream.

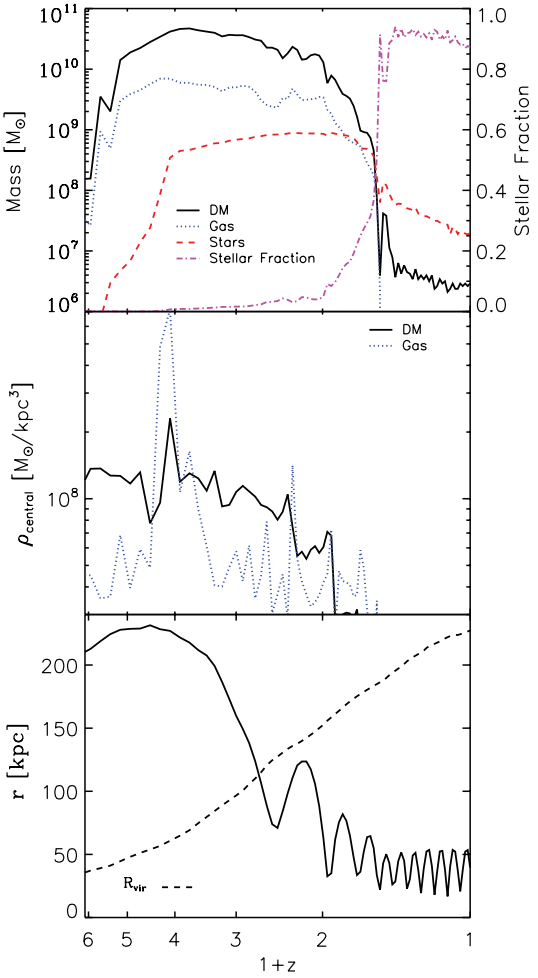

Figure 10. Top panel: the mass in dark matter (black, solid), gas (blue, dotted) and stars (red, dashed) gravitationally bound to the satellite's main progenitor, and the stellar fraction (magenta, dot–dashed, measured on the right vertical axis) as a function of redshift. Some of the small variations in the masses (and hence also the stellar fraction) at $z < 1$ are due to the difficulty in identifying the subhalo's particles against the high background density at the centre of the main halo. Centre panel: the density of dark matter (black, solid) and gas (blue, dotted) within the central 1 kpc. Bottom panel: the distance to the satellite from the centre of the main halo. The dashed line indicates the virial radius of the main halo.

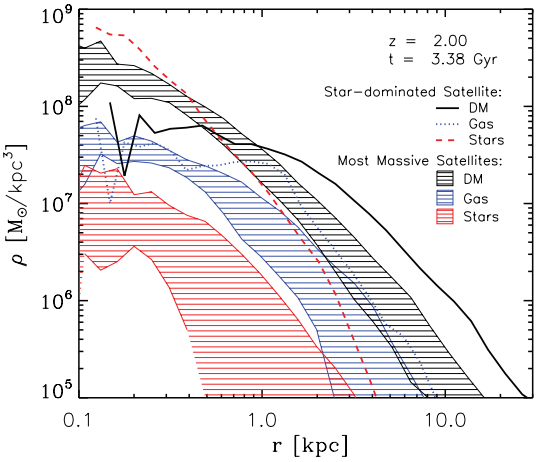

Figure 11. The dark matter (black, solid), gas (blue, dotted) and stellar (red, dashed) density profiles of the galaxy at $z \sim 2$, when it is first accreted as a satellite. Regions of the same colour indicate the spread of values ($\pm 1\sigma$) in each radial bin for the nine most massive surviving satellites at $z = 0$.

and gas have shallower than average central density profiles. It is unclear how much effect the gravitational softening has in this respect, since forces begin to become sub-Newtonian on scales less than $\lesssim$720 pc, but we note that the profiles also differ outside that radius. The highly 'cusped' stellar profile allows the central stellar nucleus to resist the strong tidal forces that unbind the majority of the dark matter. It also accounts for the unusually small half-light radius shown in Fig. 6.

The origin of these density profiles is related to the satellite's atypical formation history. In a series of major mergers at $z \sim 3$, gas is funnelled to the centre of the main progenitor, initiating an intense burst of star formation that gives rise to a highly concentrated stellar distribution. The subsequent burst of feedback energy rapidly removes a large fraction of the gas and leads to a fall in the mean binding energy of the central ($r < 1$ kpc) dark matter. This episode is clearly visible in the middle panel of Fig. 10, which shows the central gas density (blue curve) increases sharply and then drops back to the pre-merger value as gas is expelled by feedback and turned into stars, followed by a decline in the dark matter density (black curve) in response to the change in the potential. This sequence of events is effectively the process originally proposed by Navarro et al. (1996a). The reduced binding energy of its central dark matter, along with an extreme orbit, combine to produce the unusual properties of this satellite at $z = 0$.

7 CONCLUSIONS

We have investigated the formation and evolution of a MW-like satellite system in an SPH simulation over three levels of resolution, in which particle masses vary by a factor of 64. The properties of our simulated satellites show relatively good numerical convergence, with the final stellar masses typically agreeing to within a factor of 2, and always to within a factor of 6. We also compared to an independent estimate of the stellar mass expected to form in each subhalo, using the semi-analytical model of C10. The two theoretical techniques produce a similar ranking of the subhaloes by stellar mass, although our simulations typically form a higher mass of stars by a factor of between 2 and 6. This discrepancy may be partly explained by the assumption in the semi-analytical model that gas is stripped instantaneously when a galaxy becomes a satellite. The mass evolution in gas, stars and dark matter of each satellite agrees well between resolutions, except that gas is stripped more rapidly at lower resolution following accretion on to the main halo. Poorer force resolution causes gas particles to be more loosely bound to the subhalo and hence more susceptible to ram pressure stripping. This phenomenon may account for many of the differences in the final stellar masses between resolutions. Despite the inclusion of measures to improve SPH's modelling of contact instabilities, it is likely that our code still underestimates ram pressure stripping. Satellites will therefore retain more gas and form more stars after accretion than they should do.

By comparing the dark matter haloes of our satellite galaxies to those that form in a dissipationless version of the same simulation, we were able to quantify the expected impact of baryons on the phase-space structure of the dark matter. Due to small deviations in satellite orbits between different realizations of the same halo, it is necessary to make this comparison when the satellite first falls in rather than at $z = 0$. Although in some radial bins, in a few

subhaloes, the density and velocity dispersion profiles are found to change by ∼30 per cent, the differences were typically less than 10 per cent. With the caveat that the resolution of our simulation may limit the magnitude of such effects, we conclude that baryons have a relatively small impact on the structure of the dark matter haloes of satellite galaxies around MW-like hosts. We note that several previous studies have found that baryonic mechanisms can reduce the central dark matter densities of dwarf galaxies appreciably (e.g. Navarro et al. 1996a; El-Zant et al. 2001; Read & Gilmore 2005; Mashchenko et al. 2006; Goerdt et al. 2010; Governato et al. 2010); however, we find evidence for such effects only in one satellite. Our model provides a reasonable match to the faint end of the Local Group satellite luminosity function averaged between the MW and M31, although there is a slight deficit at the bright end, with no LMC analogue. However, SDSS data (Guo et al. 2011; Liu et al. 2011; Tollerud et al. 2011) suggest that it is quite common for galaxies with luminosities like the MW to have no satellites as bright as the LMC and SMC. The underestimation of ram pressure stripping and the corresponding overestimation of total stellar mass described above may increase the disagreement with the observations at the bright end. Effectively this means that less of the energy available from SNe would be required in order to match the observed satellite luminosity function.

Due to the limitations of the spatial resolution and the implementation of baryonic physics in our simulations, particularly the modelling of the multiphase ISM, stars do not form in sufficiently concentrated distributions to match the half-light radii of Local Group satellites. However, the reasonable agreement between the stellar masses in simulations with different resolution and different modelling techniques, combined with the match to the observed satellite luminosity function, suggests that the baryonic mass that is able to cool in each (sub)halo and form stars is realistic.

In order to test whether satellites of a given luminosity form in haloes with masses consistent with those observed, we compare their 'half-light masses' with values derived for a selection of the brightest MW satellites by Wolf et al. (2010). For this comparison, each satellite is assigned a distribution of half-light radii from the best fit to the observed luminosity–size relation and its variance. In the hydrodynamical simulation, the gravitational softening is comparable to these fitted half-light radii, so we instead measure the masses in a much higher resolution, DMO realization of the simulation. We hence explicitly ignore any effects baryons may have had on the central density profiles, which, in any case, the results in Section 3 suggest are small. The large scatter about the observed relation translates into a broad range of possible masses for each simulated satellite, but none the less, the mean masses for the brightest examples ($M_V < -11$) are about three to five times higher than their observed counterparts. The observed mass–luminosity relation seems to be somewhat steeper than that produced by our model, although due to the small sample sizes, the slope of the relation and the scatter about it are relatively poorly defined in both cases. A KS test, taking into account the uncertainties in the half-light radii assigned to the simulated satellites, returns a 6 per cent probability that the observed masses could have been drawn from the distribution defined by the simulation data. We note that this result is robust to small changes in the satellite luminosities due to the underestimation of ram pressure stripping; assigning a smaller half-light radius to a satellite also reduces the central mass measured, such that the discrepancy between the simulated and observed satellites remains.

Although the apparent disagreement between the simulations and the data could be simply due to statistics, there are also a number of plausible physical explanations. It could be that baryonic processes significantly reduce the central dark matter densities of satellite galaxies. Possible mechanisms to achieve this include, for instance, a sudden change in the local potential, induced by the rapid expulsion of baryonic mass through stellar feedback (e.g. Navarro et al. 1996a) or heating due to bulk motions of dense clumps of gas (e.g. Mashchenko et al. 2006). The results in Section 3 imply that, if such processes are important, they are either not resolved in the Aq-C-4 simulation or not properly captured by our feedback prescription, except in one case, which happens to be the most massive subhalo at accretion. Less concentrated dark matter profiles would also result if the dark matter consists of warm, rather than cold, particles (e.g. Lovell et al. 2011).

The broad range of possible explanations of the discrepancy highlighted by our results illustrates how uncertain our understanding of galaxy formation still is on the scale of dwarf galaxies. Determining which, if any, is correct will be of critical importance in assessing the viability of the CDM cosmology and the success of galaxy formation models.

ACKNOWLEDGMENTS

We thank Joop Schaye for helpful comments in the early stages of this work and Adrian Jenkins for creating the initial conditions for the simulations. We are also grateful to Andrew Cooper for giving us access to his semi-analytical satellite data and for helpful discussions. OHP acknowledges the receipt of an STFC studentship. TO acknowledges financial support by Grant-in-Aid for Scientific Research (S) by JSPS (20224002) and by Grant-in-Aid for Young Scientists (start-up: 21840015). Our thanks to the anonymous referee for several helpful suggestions that improved the manuscript. Simulations associated with this work were run on the IBM pSeries Power6 at the Rechenzentrum, Garching, the Cosmology Machine at the Institute for Computational Cosmology (ICC) in Durham, the Cray XT4 at the National Astronomical Observatory of Japan's Centre for Computational Astrophysics and at the Centre for Computational Sciences in the University of Tsukuba. CSF acknowledges a Royal Society Wolfson research merit award. We thank the DEISA Consortium (www.deisa.eu), co-funded through the EU FP6 project RI-031513 and the FP7 project RI-222919, for support within the DEISA Extreme Computing Initiative. This work was supported in part by an STFC rolling grant to the ICC and ERC Advanced Investigator grant 267291 COSMIWAY.

REFERENCES

Abel T., Haehnelt M. G., 1999, ApJ, 520, L13
Agertz O. et al., 2007, MNRAS, 380, 963
Bate M. R., Burkert A., 1997, MNRAS, 288, 1060
Belokurov V. et al., 2007, ApJ, 654, 897
Benson A. J., Frenk C. S., Lacey C. G., Baugh C. M., Cole S., 2002, MNRAS, 333, 177
Blumenthal G. R., Faber S. M., Flores R., Primack J. R., 1986, ApJ, 301, 27
Bothun G. D., Thompson I. B., 1988, AJ, 96, 877
Bower R. G., Benson A. J., Malbon R., Helly J. C., Frenk C. S., Baugh C. M., Cole S., Lacey C. G., 2006, MNRAS, 370, 645
Boylan-Kolchin M., Bullock J. S., Kaplinghat M., 2011, MNRAS, 415, L40
Ceverino D., Klypin A., 2009, ApJ, 695, 292
Ceverino D., Dekel A., Bournaud F., 2010, MNRAS, 404, 2151
Chabrier G., 2003, PASP, 115, 763
Cooper A. P. et al., 2010, MNRAS, 406, 744 (C10)
Dalla Vecchia C., Schaye J., 2008, MNRAS, 387, 1431
Davis M., Efstathiou G., Frenk C. S., White S. D. M., 1985, ApJ, 292, 371

Dehnen W., McLaughlin D. E., Sachania J., 2006, MNRAS, 369, 1688
Diemand J., Kuhlen M., Madau P., Zemp M., Moore B., Potter D., Stadel J., 2008, Nat, 454, 735
Dolag K., Borgani S., Murante G., Springel V., 2009, MNRAS, 399, 497
El-Zant A., Shlosman I., Hoffman Y., 2001, ApJ, 560, 636
El-Zant A. A., Hoffman Y., Primack J., Combes F., Shlosman I., 2004, ApJ, 607, L75
Elmegreen B. G., 1989, ApJ, 338, 178
Ferland G. J., Korista K. T., Verner D. A., Ferguson J. W., Kingdon J. B., Verner E. M., 1998, PASP, 110, 761
Fioc M., Rocca-Volmerange B., 1997, A&A, 326, 950
Font A. S. et al., 2011, MNRAS, 417, 1260
Frenk C. S., Evrard A. E., White S. D. M., Summers F. J., 1996, ApJ, 472, 460
Frenk C. S., White S. D. M., Bode P., Bond J. R., Bryan G. L., Cen R., Couchman H. M. P., Evrard A. E., 1999, ApJ, 525, 554
Fukui Y., Mizuno N., Yamaguchi R., Mizuno A., Onishi T., 2001, PASJ, 53, L41
Gelato S., Sommer-Larsen J., 1999, MNRAS, 303, 321
Gilmore G., Wilkinson M. I., Wyse R. F. G., Kleyna J. T., Koch A., Evans N. W., Grebel E. K., 2007, ApJ, 663, 948
Gnedin O. Y., Hernquist L., Ostriker J. P., 1999, ApJ, 514, 109
Gnedin O. Y., Kravtsov A. V., Klypin A. A., Nagai D., 2004, ApJ, 616, 16
Goerdt T., Moore B., Read J. I., Stadel J., Zemp M., 2006, MNRAS, 368, 1073
Goerdt T., Moore B., Read J. I., Stadel J., 2010, ApJ, 725, 1707
Governato F. et al., 2010, Nat, 463, 203
Guo Q., Cole S., Eke V., Frenk C., 2011, MNRAS, 417, 370
Haardt F., Madau P., 2001, in Neumann, D. M., Tran, J. T. V., eds, Clusters of Galaxies and the High Redshift Universe Observed in X-rays. Editions Frontières, Paris, p. 64
Heyer M. H., Carpenter J. M., Snell R. L., 2001, ApJ, 551, 852
Hilditch R. W., Howarth I. D., Harries T. J., 2005, MNRAS, 357, 304
Hoeft M., Yepes G., Gottlöber S., Springel V., 2006, MNRAS, 371, 401
Hogan C. J., Dalcanton J. J., 2000, Phys. Rev. D, 62, 063511
Katz N., Weinberg D. H., Hernquist L., 1996, ApJS, 105, 19
Kawata D., Okamoto T., Cen R., Gibson B. K., 2009, preprint (arXiv e-prints)
Kennicutt R. C., Jr, 1998, ApJ, 498, 541
Klypin A., Kravtsov A. V., Valenzuela O., Prada F., 1999, ApJ, 522, 82
Knebe A., Libeskind N. I., Knollmann S. R., Martinez-Vaquero L. A., Yepes G., Gottlöber S., Hoffman Y., 2011a, MNRAS, 412, 529
Knebe A. et al., 2011b, MNRAS, 415, 2293
Kolmogorov A., 1933, G. Istituto Ital. Attuari, 4, 83
Koposov S., Belokurov V., Evans N. W., Hewett P. C., Irwin M. J., 2008, ApJ, 686, 279
Li Y., White S. D. M., 2008, MNRAS, 384, 1459
Li Y., De Lucia G., Helmi A., 2010, MNRAS, 401, 2036
Liu L., Gerke B. F., Wechsler R. H., Behroozi P. S., Busha M. T., 2011, ApJ, 733, 62
Lovell M. et al., 2011, preprint (arXiv e-prints)
Macciò A. V., Kang X., Fontanot F., Somerville R. S., Koposov S., Monaco P., 2010, MNRAS, 402, 1995
McConnachie A. W. et al., 2008, ApJ, 688, 1009
Machacek M. E., Bryan G. L., Abel T., 2001, ApJ, 548, 509
Marigo P., 2001, A&A, 370, 194
Martin C. L., 2005, ApJ, 621, 227
Martin N. F., Ibata R. A., Irwin M. J., Chapman S., Lewis G. F., Ferguson A. M. N., Tanvir N., McConnachie A. W., 2006, MNRAS, 371, 1983
Mashchenko S., Couchman H. M. P., Wadsley J., 2006, Nat, 442, 539
Mashchenko S., Wadsley J., Couchman H. M. P., 2008, Sci, 319, 174
Mayer L., Governato F., Colpi M., Moore B., Quinn T., Wadsley J., Stadel J., Lake G., 2001, ApJ, 547, L123
Mihos J. C., Hernquist L., 1994, ApJ, 437, 611
Mo H. J., Mao S., 2004, MNRAS, 353, 829
Moore B., Ghigna S., Governato F., Lake G., Quinn T., Stadel J., Tozzi P., 1999, ApJ, 524, L19
Navarro J. F., White S. D. M., 1993, MNRAS, 265, 271
Navarro J. F., Eke V. R., Frenk C. S., 1996a, MNRAS, 283, L72
Navarro J. F., Frenk C. S., White S. D. M., 1996b, ApJ, 462, 563
Navarro J. F., Frenk C. S., White S. D. M., 1997, ApJ, 490, 493
Navarro J. F. et al., 2010, MNRAS, 402, 21
Okamoto T., Frenk C. S., 2009, MNRAS, 399, L174
Okamoto T., Jenkins A., Eke V. R., Quilis V., Frenk C. S., 2003, MNRAS, 345, 429
Okamoto T., Gao L., Theuns T., 2008, MNRAS, 390, 920
Okamoto T., Frenk C. S., Jenkins A., Theuns T., 2010, MNRAS, 406, 208
Peñarrubia J., Navarro J. F., McConnachie A. W., 2008, ApJ, 673, 226
Pietrzyński G. et al., 2009, ApJ, 697, 862
Pontzen A., Governato F., 2011, preprint (arXiv e-prints)
Portinari L., Chiosi C., Bressan A., 1998, A&A, 334, 505
Power C., Navarro J. F., Jenkins A., Frenk C. S., White S. D. M., Springel V., Stadel J., Quinn T., 2003, MNRAS, 338, 14
Price D. J., 2008, J. Comput. Phys., 2271, 10040
Read J. I., Gilmore G., 2005, MNRAS, 356, 107
Robertson B. E., Kravtsov A. V., 2008, ApJ, 680, 1083
Saitoh T. R., Makino J., 2009, ApJ, 697, L99
Samland M., Gerhard O. E., 2003, A&A, 399, 961
Sánchez-Salcedo F. J., Reyes Iturbide J., Hernandez X., 2006, MNRAS, 370, 1829
Sawala T., Scannapieco C., White S., 2011, preprint (arXiv e-prints)
Schaye J., Dalla Vecchia C., 2008, MNRAS, 383, 1210
Schaye J. et al., 2010, MNRAS, 402, 1536
Sijacki D., Vogelsberger M., Keres D., Springel V., Hernquist L., 2011, preprint (arXiv e-prints)
Smirnov N., 1939, Bul. Math. l'Universite Moscou, 2, 3
Solomon P. M., Rivolo A. R., 1989, ApJ, 339, 919
Somerville R. S., 2002, ApJ, 572, L23
Springel V., 2010, ARA&A, 48, 391
Springel V., Hernquist L., 2003, MNRAS, 339, 289
Springel V., White S. D. M., Tormen G., Kauffmann G., 2001, MNRAS, 328, 726
Springel V. et al., 2008, MNRAS, 391, 1685
Stadel J., Potter D., Moore B., Diemand J., Madau P., Zemp M., Kuhlen M., Quilis V., 2009, MNRAS, 398, L21
Stoehr F., White S. D. M., Tormen G., Springel V., 2002, MNRAS, 335, L84
Strigari L. E., Bullock J. S., Kaplinghat M., Kravtsov A. V., Gnedin O. Y., Abazajian K., Klypin A. A., 2006, ApJ, 652, 306
Strigari L. E., Frenk C. S., White S. D. M., 2010, MNRAS, 408, 2364
Tollerud E. J., Boylan-Kolchin M., Barton E. J., Bullock J. S., Trinh C. Q., 2011, ApJ, 738, 102
Truelove J. K., Klein R. I., McKee C. F., Holliman J. H., II, Howell L. H., Greenough J. A., 1997, ApJ, 489, L179
Wada K., Norman C. A., 2007, ApJ, 660, 276
Wadepuhl M., Springel V., 2011, MNRAS, 410, 1975
Walker M. G., Mateo M., Olszewski E. W., Gnedin O. Y., Wang X., Sen B., Woodroofe M., 2007, ApJ, 667, L53
Walker M. G., Mateo M., Olszewski E. W., Peñarrubia J., Wyn Evans N., Gilmore G., 2009, ApJ, 704, 1274
Watkins L. L., Evans N. W., An J. H., 2010, MNRAS, 406, 264
Wiersma R. P. C., Schaye J., Smith B. D., 2009a, MNRAS, 393, 99
Wiersma R. P. C., Schaye J., Theuns T., Dalla Vecchia C., Tornatore L., 2009b, MNRAS, 399, 574
Wolf J., Martinez G. D., Bullock J. S., Kaplinghat M., Geha M., Muñoz R. R., Simon J. D., Avedo F. F., 2010, MNRAS, 406, 1220
Xue X. X. et al., 2008, ApJ, 684, 1143
York D. G. et al., 2000, AJ, 120, 1579
Zucker D. B. et al., 2004, ApJ, 612, L121

This paper has been typeset from a TEX/LATEX file prepared by the author.